Phys Chem Minerals (2012) 39:613–626
DOI 10.1007/s00269-012-0516-x

ORIGINAL PAPER

Crystallographic preferred orientation in wüstite (FeO) through the cubic-to-rhombohedral phase transition

P. Kaercher · S. Speziale · L. Miyagi · W. Kanitpanyacharoen · H.-R. Wenk

Received: 30 January 2012 / Accepted: 27 May 2012 / Published online: 26 July 2012
© Springer-Verlag 2012

Abstract Magnesiowüstite, $(Mg_{0.08}Fe_{0.88})O$, and wüstite, $Fe_{0.94}O$, were compressed to ~36 GPa at ambient temperature in the diamond anvil cell (DAC) at the Advanced Light Source. X-ray diffraction patterns were taken in situ in radial geometry in order to study the evolution of crystallographic preferred orientation through the cubic-to-rhombohedral phase transition. Under uniaxial stress in the DAC, $\{100\}_c$ planes aligned perpendicular to the compression direction. The $\{100\}_c$ in cubic became $\{01\bar{1}2\}_r$ in rhombohedral and remained aligned perpendicular to the compression direction. However, the $\{101\}_c$ and $\{111\}_c$ planes in the cubic phase split into $\{10\bar{1}4\}_r$ and $\{11\bar{2}0\}_r$, and $(0001)_r$ and $\{10\bar{1}1\}_r$, respectively, in the rhombohedral phase. The $\{11\bar{2}0\}_r$ planes preferentially aligned perpendicular to the compression direction while $\{10\bar{1}4\}_r$ oriented at a low angle to the compression direction. Similarly, $\{10\bar{1}1\}_r$ showed a slight preference to align more closely perpendicular to the compression direction than $(0001)_r$. This variant selection may occur because the $\langle 10\bar{1}4\rangle_r$ and $[0001]_r$ directions are the softer of the two sets of directions. The rhombohedral texture distortion may also be due to subsequent deformation. Indeed, polycrystal plasticity simulations indicate that for preferred $\{10\bar{1}4\}\langle 1\bar{2}10\rangle_r$ and $\{11\bar{2}0\}\langle\bar{1}101\rangle_r$ slip and slightly less active $\{10\bar{1}1\}\langle\bar{1}2\bar{1}0\rangle_r$ slip, the observed texture pattern can be obtained.

Keywords Wüstite · Preferred orientation · Diamond anvil cell · Phase transition

P. Kaercher · W. Kanitpanyacharoen · H.-R. Wenk (✉)
Department of Earth and Planetary Science,
University of California, Berkeley, CA 94720, USA
e-mail: wenk@berkeley.edu

S. Speziale
Helmholtz Center, GFZ German Research Centre
for Geosciences, 14473 Potsdam, Germany

L. Miyagi
Department of Geology and Geophysics, University of Utah,
Salt Lake City, UT 84112, USA

Introduction

As one of the major lower-mantle mineral phases along with $(Mg,Fe)SiO_3$ perovskite, the mechanical properties of $(Mg_xFe_{1-x})O$ [hereafter referred to as (Mg,Fe)O] at high pressure have implications for the rheology and composition of the lower mantle (Jeanloz and Thompson 1983). For instance, preferred orientation of (Mg,Fe)O crystals due to differential stress may contribute to localized areas of seismic anisotropy in down-going slabs and upwelling plumes in the convecting lower mantle. This is because large strain from mantle convection is at least partially accommodated by propagation of dislocations along slip planes (Wenk et al. 2011). In turn, this leads to lattice rotation and ultimately crystallographic preferred orientation (texture) that causes seismic waves to travel faster in some directions than in others. Comparison of seismic data with mineral physics helps constrain the composition of the lower mantle.

Electric and magnetic properties of (Mg,Fe)O at depth are also important, and hence, the effect of pressure on the electronic structure of Fe in (Mg,Fe)O has been the subject of intense research. At ambient conditions, (Mg,Fe)O crystallizes in a face-centered cubic (B1) structure consisting of a close-packed O-sublattice with Mg and Fe occupying octahedral interstices. Due to such a simple structure based on one single coordination polyhedron for the cation species, even subtle changes at the Fe-site have a

visible effect on the properties of the whole material, sometimes at moderately low Fe contents. Changes in the electronic structure of Fe at high pressure can affect the magnetic properties of (Mg,Fe)O (e.g., Pasternak et al. 1997; Badro et al. 1999), for example, a spin collapse crossover at pressures above 40 GPa, depending on Fe content (Gramsch et al. 2003; Speziale et al. 2005; Fei et al. 2007; Lin et al. 2003, 2005a, b; Mao et al. 2011). Compositions with greater Fe content remain in the high spin state to higher pressure, implying partitioning of Fe from (Mg,Fe)SiO_3 to (Mg,Fe)O with depth, which may (Cohen et al. 1997; Badro et al. 2003) or may not (Irifune et al. 2010) result in a seismically stratified lower mantle. In addition, the outer core may also be seismically stratified due to magnetic collapse of Fe^{2+} dissolved in Fe-rich liquid (Cohen et al. 1997). Furthermore, it was recently discovered that a metallic cubic phase of FeO exists at pressures and temperatures corresponding to the core-mantle-boundary which would affect the way the magnetic field is propagated to Earth's surface (Ohta et al. 2012). Electronic changes in Fe can also affect the elastic constants at high pressure (Crowhurst et al. 2008; Marquardt et al. 2009; Antonangeli et al. 2011). Lin et al. (2009) observed no change in preferred orientation in polycrystalline $(Mg_{0.83}Fe_{0.17})O$ as pressure increased through the spin transition, suggesting that magnetic changes do not cause changes in deformation mechanisms in Fe-rich compositions of the MgO-FeO solid-solution series.

Several structural changes in FeO occur at pressure, one of which is perhaps due to magnetic and elastic changes. Recent X-ray diffraction experiments suggest a transition from a B1 (NaCl) to a B2 (CsCl) structure at outer core conditions (above 230 GPa and 2,500–5,000 K) (Ozawa et al. 2011). A more established phase transition to a B8 (NiAs), an anti-B8 structure, or a polytypical combination of the two occurs at pressures above 70 GPa (Jackson and Ringwood 1981; Fei and Mao 1994; Mazin et al. 1998; Murakami et al. 2004). At much lower pressure near 10–20 GPa, another well-studied phase transition from cubic-to-rhombohedral symmetry in magnesiowüstite (Mg,Fe)O has been observed in the diamond anvil cell (DAC) (Zou et al. 1980; Mao et al. 1996; Shu et al. 1998). The rhombohedral distortion occurs via extension of one cube body diagonal and shortening of the other three (Fig. 1) at a pressure that depends on the degree of non-hydrostaticity in the sample chamber (Zou et al. 1980; Jeanloz and Sato-Sorensen 1986; Dubrovinsky et al. 2000) and Fe content of the sample (Lin et al. 2003; Kondo et al. 2004; Kantor et al. 2006; Zhuravlev et al. 2010). In fact, it is debatable whether the cubic-to-rhombohedral transition even occurs for compositions with Fe $\leq$ 20 % (Jacobsen et al. 2004; Kondo et al. 2004; Kantor et al. 2006), and it

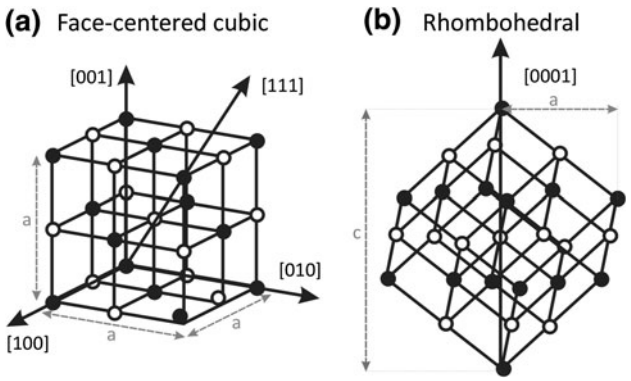

Fig. 1 Structure of FeO in **a** cubic and **b** hexagonal reference frames. The $[111]_c$ direction in cubic becomes the $[0001]_r$ hexagonal crystallographic axis

has never been found to occur in pure periclase (MgO) (Duffy et al. 1995). The absence of a rhombohedral phase in MgO points to electronic changes in Fe as the driving mechanism for the transition in (Mg,Fe)O. Indeed, experimental studies have found a paramagnetic-to-antiferromagnetic transition in wüstite near 5 GPa (Zou et al. 1980; Kantor et al. 2004a, b). Some studies propose that this magnetic transition causes the extreme softening of C_{44} found both with experiments (Jackson et al. 1990; Mao et al. 1996, 2002) and ab initio calculations (Koči et al. 2007) and thus is ultimately responsible for the structural phase transition (Yagi et al. 1985; Jackson et al. 1990). Others suggest that they do not correlate (Kantor et al. 2004a, b, 2007; Ding et al. 2005).

Despite the number of studies examining the physical changes in (Mg,Fe)O with pressure and temperature, this is the first study to investigate changes in preferred orientation through the cubic-to-rhombohedral phase transition. We did so by performing in situ synchrotron X-ray diffraction in the radial DAC. We then investigated slip system activities that lead to the observed texture using viscoplastic self-consistent (VPSC) modeling in order to gain further insight into the transition.

Experiments

Synthesized powders of magnesiowüstite $(Mg_{0.08}Fe_{0.88})O$ and wüstite $(Fe_{0.94}O)$ were compressed to $\sim$36 GPa in the DAC in X-ray diffraction experiments at beamline 12.2.2 of the Advanced Light Source at Lawrence Berkeley National Laboratory. We performed experiments in radial geometry (Wenk et al. 2006) rather than axial geometry in order to see variations in diffraction intensities as a function of the azimuthal angle η on Debye rings (the angle with respect to the plane of the diamond anvil culets) which indicates preferred orientation of the lattice in the crystal

aggregate. No pressure medium was used in order to impose deviatoric stress in addition to hydrostatic pressure.

Magnesiowüstite $(Mg_{0.08}Fe_{0.88})O$

A powder sample of $(Mg_{0.08}Fe_{0.88})O$, the same as sample 10−1 in Bonczar and Graham (1982), also used in Speziale et al. (2005, 2007), was prepared by sintering a mixture of MgO, Fe_2O_3, and Fe at ~1,000 °C as described in Bonczar and Graham (1982). Chemical composition was quantified with wet chemical analysis. The sample was loaded into an X-ray-transparent boron-epoxy gasket inside of a kapton sheet. The sample chamber was ~80 μm in diameter and ~50 μm deep. A ~5-μm-thick gold flake ~15 μm in diameter was placed in the sample chamber and used as a pressure calibrant, applying the equation of state (EOS) for Au (Shim et al. 2002). The diamond culets were 300 μm in diameter. A modified Mao-Bell DAC with large lateral openings for radial diffraction was loaded into a holding frame where pressure was increased with a lever arm operated by a single screw. The sample was placed ~129 mm from the detector, and a monochromatic X-ray of wavelength 0.354241 Å was collimated to a beamsize of 10 μm × 10 μm and focused onto the sample. Diffraction images were collected for 20 s on a Bruker PT200 charge-coupled device (CCD). Instrument parameters, such as sample-to-detector distance, beam center, and detector tilt, were calibrated using a LaB_6 standard.

Wüstite $(Fe_{0.94}O)$

A similar experiment was performed with $Fe_{0.94}O$ powder prepared by heating Fe_2O_3 to 1,473 K in a $CO–CO_2$ mixing furnace to control oxygen fugacity as described in Fei (1996). Fei (1996) characterized sample non-stoichiometry by measuring the lattice parameter with X-ray diffraction and found $a = 4.307(1)$ corresponding to a ~6 % iron vacancy (Hazen 1981). Iron-rich compositions in the MgO–FeO solid solution have complex defect structures and are invariably non-stoichiometric (Jeanloz and Sato-Sorensen 1986). To help account for this non-stoichiometry in the analysis of the data, we have used the elastic constants for a sample with similar iron vacancy, $Fe_{0.945}O$ (Jackson et al. 1990). An X-ray-transparent kapton/boron-epoxy gasket with a sample chamber 80 μm in diameter and 50 μm deep was used. A small flake of Pt (Alfa Aesar foil ~20 μm in diameter and 5 μm thick) was embedded in the sample and used as a pressure indicator using the EOS for Pt (Menendez-Proupin and Singh 2007). Diamond culet diameter was again 300 μm. A nitrogen gas pressure membrane was used to apply pressure and uniaxial stress to the sample inside of a Mao-Bell DAC. The sample was placed ~345 mm from a MAR345 image plate detector, and diffraction patterns were collected for 120 s with a 0.49594 Å wavelength X-ray beam 10 μm in diameter. A LaB_6 powder standard was used to calibrate instrument parameters.

Data analysis

Rietveld refinement (Rietveld 1969), a least squares method, was implemented in the software package MAUD (Lutterotti et al. 1997) to find a calculated fit to experimentally collected diffraction patterns. By calculating the best fit to hydrostatic peak position, that is at azimuthal angle $\eta = 54.7°$ from the compression direction (Singh et al. 1998; Merkel et al. 2009), we determined the cell parameters and thus the volume of the unit cell. In addition, peak width, sinusoidal variations of peak position in 2θ, and regular changes in peak intensity (Fig. 2) were fit in order to find the crystallite size and root mean square (rms) microstrain, differential stress, and preferred orientation, respectively.

Crystallite size and rms microstrain were both calculated assuming an isotropic grain size. The rms microstrain

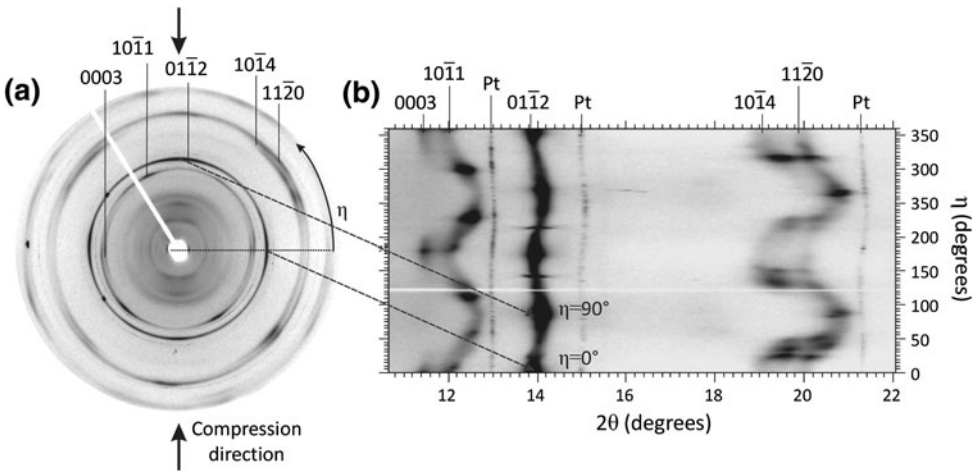

Fig. 2 **a** Diffraction image of $Fe_{0.94}O$ collected at 36 GPa in the rhombohedral phase. The diffraction rings are labeled with hexagonal *hkil* indices. The *solid curved arrow* shows the direction of increasing angle η. Compression direction is *vertical* (*arrows*). **b** Image in **a** has been unrolled. *Dashed arrows* show corresponding areas of maximum intensity of the $01\bar{1}2_r$ Debye ring/peak. The *white horizontal streak* is from the beamstop

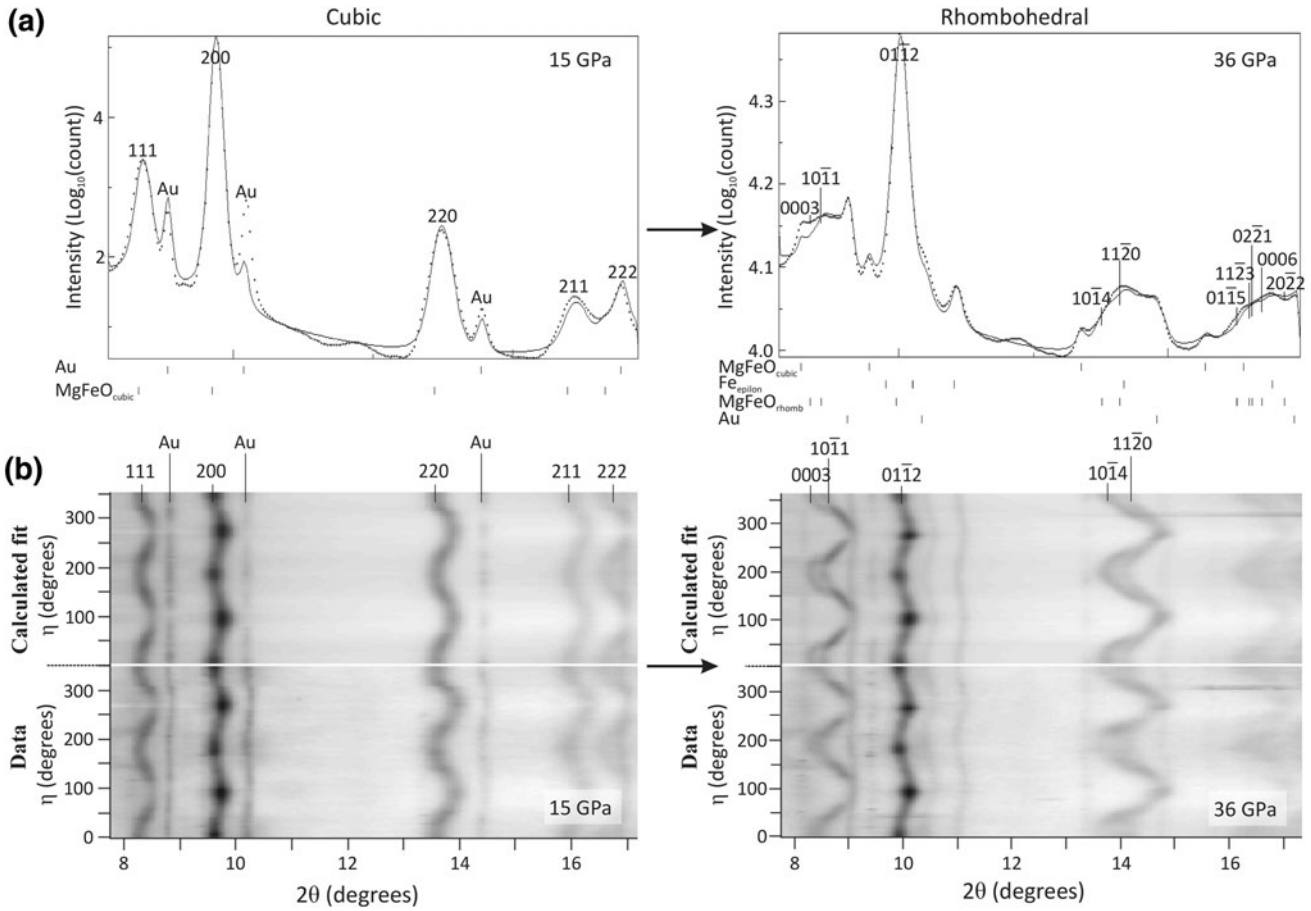

Fig. 3 **a** Peak profiles for $(Mg_{0.08}Fe_{0.88})O$ at 15 GPa (*left*) and 36 GPa (*right*). The phase transition from face-centered cubic to rhombohedral is marked by splitting of both the 111_c and the 220_c peaks, but not the 200_c peak. The experimental spectrum is shown with a *dashed line*, and the calculated fit is shown with a *solid line*. *Tick* marks below the profiles (*top*) denote peak locations for the phases labeled to the *left*. Small cubic peaks, diffracted from sample which spilled outside the sample chamber, are present in the rhombohedral phase but are not labeled in the 36 GPa spectra. **b** Unrolled diffraction images. The *bottom* half of each pattern is the experimental data and the *top* is the calculated fit. Notice the strong texture of the 0003_r peak, making it visible only at angles η near 0° and 180°

(hereafter referred to as microstrain), the average lattice distortion due to plastic strain in a crystal, was calculated from the width of the Gaussian component of the Voigt function that was used to fit our diffraction peaks (Lutterotti and Scardi 1990).

Periodic variations in both peak position and intensity are best seen by unrolling Debye rings. This was done in Fit2D (Hammersley et al. 1996), and diffraction intensity was integrated every 5° in η for a total of 72 spectra (Fig. 2). Integrated diffraction spectra (Fig. 3a) and corresponding 2D plots (Fig. 3b) with experimental diffraction patterns (bottom) and the calculated fit (top) are shown for the cubic (left) and rhombohedral phases (right).

Stress

The diamond anvils and gasket imposed both hydrostatic pressure and uniaxial stress on the sample. The hydrostatic stress component is determined as a function of volume change (i.e., peak position in the diffraction pattern) of Au and Pt that were used as calibrants. Here, we used the EOS of the calibrants rather than the sample itself since the EOS of the rhombohedral phase for any composition of (Mg,Fe)O is unknown.

Because no pressure medium is used, the sample is subject to non-hydrostatic conditions. Sinusoidal variations in peak positions with respect to the compression direction (Fig. 3b) indicate that deviatoric stress imposed by the DAC has caused the sample to strain elastically. Elastic strain, unlike plastic strain, is reversible deformation in which bonds are stretched but not broken. Deviatoric stress, the stress experienced in different crystallographic directions, can be calculated from the non-isotropic elastic strain and the single crystal elastic constants. Since the latter are yet unknown for the rhombohedral phase, deviatoric stress could only be determined for the cubic phase.

Differential stress t in the cubic phase was calculated from the principal stresses σ_{11} and σ_{33} using the relationship $t = \sigma_{33} - \sigma_{11}$ (Singh et al. 1998). Principal stresses σ_{11} and σ_{33} for the cubic phase were found using the Moment Pole Stress model (Matthies et al. 2001) implemented in MAUD which uses the elastic constants of $Fe_{0.945}O$ as a function of pressure (Jackson et al. 1990) as input and the BulkPathGeo stress/strain model (Matthies et al. 2001) to fit the strain. Deviatoric stress can then be calculated from the differential stress t:

$$\delta\sigma_{ij} = \begin{bmatrix} t/3 & 0 & 0 \\ 0 & t/3 & 0 \\ 0 & 0 & -2t/3 \end{bmatrix}$$

where the uniaxial stress is applied in the x_3 direction (corresponding to the compression axis in the DAC), and the stress distribution is assumed to be cylindrically symmetric about the compression axis such that $\sigma_{11} = \sigma_{22}$. In this study, we use the standard convention of defining compressive stresses as negative and extensional stresses as positive.

Because elastic constants are not known for the rhombohedral phase, the radial diffraction in the DAC approach of Singh et al. (1998), as implemented in MAUD, was used to fit elastic strain. As seen in Fig. 3, some peaks exhibited much higher lattice strain than others (e.g., $10\bar{1}1$), and Singh's model is able to fit the strain in each peak individually by refining the parameter $Q(hkl)$ (defined in Singh et al. 1998). The parameter $Q(hkl)$ is related to the change in d-spacings produced from deviatoric stress by

$$d_m(hkl) = d_p(hkl)[1 + (1 - 3\cos\psi^2)Q(hkl)]$$

where $Q(hkl) = \frac{t}{3}\left(\frac{\alpha}{2G_R^X(hkl)} + \frac{1-\alpha}{2G_V}\right)$, d_m are the measured lattice d-spacings, d_p are the lattice d-spacings under hydrostatic pressure, α is a weighting factor between 0 and 1, $G_R^X(hkl)$ is the aggregate shear modulus (limited to the crystallites that contribute to the recorded diffraction effect) calculated under the Reuss (iso-stress) condition, and G_V is the shear modulus under the Voigt (iso-strain) condition. Differential stress t can be determined from $Q(hkl)$ if the elastic anisotropy of the phase is known (Singh et al. 1998; Merkel et al. 2002).

Texture

Systematic variations in peak intensity with azimuth η (seen in Fig. 3) indicate crystallographic preferred orientation, or texture. Crystallographic texture was fit using E-WIMV, a tomographic algorithm similar to WIMV (Matthies and Vinel 1982) but able to compensate for irregular pole figure coverage. Pole densities in the pole figures were roughly symmetric about the compression direction as expected for DAC geometry, and thus we imposed cylindrical symmetry. The orientation distribution was calculated with a 15° resolution and subsequently smoothed with a 7.5° Gauss filter before calculating pole figures and inverse pole figures with the software BEARTEX (Wenk et al. 1998).

Results

Lattice parameters, microstrain, and differential stresses were determined at various pressures between 0 and 37 GPa for both $(Mg_{0.08}Fe_{0.88})O$ and $Fe_{0.94}O$. The results are summarized in Table 1. Our measured unit cell parameter at ambient conditions for $(Mg_{0.08}Fe_{0.88})O$ was 4.2952(1) Å, in excellent agreement with 4.2954(5) Å as measured by Bonczar and Graham (1982). The starting cell parameter for $Fe_{0.94}O$ was 4.2940 Å, 0.3 % smaller than that measured by Fei (1996). The difference is likely due to a small amount of stress applied when closing the DAC.

The phase transition from cubic ($Fm\bar{3}m$) to rhombohedral ($R\bar{3}m$) occurred near 19 GPa in both experiments, in good agreement with Yagi et al. (1985), Mao et al. (1996, 2002), and Murakami et al. (2004). The rhombohedral distortion occurs via extension of one cube body diagonal and shortening of the other three (Fig. 1). This is evidenced in the subtle change in d-spacing from cubic $d_{(111)} = 2.43$ to rhombohedral $d_{(0001)} = 2.44$ and $d_{\{10\bar{1}1\}} = 2.39$. The extended body diagonal becomes the c-axis in the rhombohedral phase where we use a hexagonal coordinate system to describe the structure.

At 19 GPa, the c/a ratio in both samples was already higher than the ideal cubic c/a ratio ($\sqrt{6} = 2.4495$, where c is a body diagonal in the cubic phase) and increased continuously to 2.5288 at 36.6 GPa in $(Mg_{0.08}Fe_{0.88})O$, and 2.5855 at 36.2 GPa in $Fe_{0.94}O$ (Table 1). The latter is similar to $c/a = 2.603$ at 38.9 GPa reported by Zou et al. (1980) for FeO. Overall c/a ratios for $Fe_{0.94}O$ were consistently higher than for $(Mg_{0.08}Fe_{0.88})O$.

Microstructure and stress

Microstrain increased with pressure in the cubic phase of $(Mg_{0.08}Fe_{0.88})O$ from 0.00428(9) at 0.6 GPa to 0.00779(7) at 13.7 GPa, then decreased across the phase transition to 0.00536(4) at 27.4 GPa, and increased again with pressure in the rhombohedral phase until the load was reduced. Microstrain increased in a similar fashion in $Fe_{0.94}O$. Microstrain was relieved by the rhombohedral distortion in both experiments, suggesting that some strain imposed by the anvils was accommodated by the displacive transition.

During compression, differential stress t changed from −0.02 GPa at 0.6 GPa to −3.14 GPa at 18.7 GPa in cubic $(Mg_{0.08}Fe_{0.88})O$ and from −0.42 at 0.2 GPa to −3.25 at

Table 1 A summary of cell parameters, *c/a* ratios, microstrain, differential stress (*t*), and texture sharpness given in m.r.d as a function of pressure and temperature in cubic (C) and rhombohedral (R) phases

Exp.	Phase	*P* (GPa)	*a* (Å)	*c* (Å)	*c/a*	Microstrain	*t* (GPa)	Pole densities	
								Min	Max
$(Mg_{0.08}Fe_{0.88})O$	C	0.6	4.2952(1)	–	–	0.00428(9)	−0.02	0.67	1.80
	C	7.4	4.2467(2)	–	–	0.00638(5)	−1.63	0.51	3.08
	C	13.7	4.2020(1)	–	–	0.00779(7)	−2.14	0.39	3.28
	C	18.7	4.141(3)	–	–	0.009(1)	−3.14	0.09	2.22
	R	18.7	2.9229(1)	7.3167(7)	2.5032	0.00642(3)	–	0.23	3.94
	R	27.4	2.8635(1)	7.2492(8)	2.5316	0.00536(4)	–	0.14	4.15
	R	36.6	2.8430(2)	7.1895(9)	2.5288	0.00634(5)	–	0.00	6.48
	C	1.8	4.276(1)	–	–	0.0054(1)	−0.01	0.25	4.24
$Fe_{0.94}O$	C	0.2	4.2940(4)	–	–	0.0033(2)	−0.42	0.64	1.84
	C	10.6	4.21783(8)	–	–	0.00541(3)	−2.21	0.31	2.69
	C	14.5	4.19488(9)	–	–	0.00644(3)	−2.58	0.31	3.15
	C	18.8	4.1720(7)	–	–	0.0040(1)	−3.25	0.19	2.64
	R	18.8	2.9184(2)	7.3659(9)	2.5240	0.00439(3)	–	0.31	2.82
	R	24.9	2.8938(1)	7.3210(5)	2.5485	0.00478(2)	–	0.26	2.93
	R	36.2	2.8278(2)	7.311(1)	2.5855	0.00600(5)	–	0.28	2.90
	C	9.1	4.2301(4)	–	–	0.00638(4)	−2.15	0.18	7.28

Minimum and maximum m.r.d for IPFs in Fig. 7 are listed in the right-most column. Numbers in parentheses are standard deviations for the last digit

Table 2 Values for the parameter $Q(hkl)$ for five crystallographic directions in the rhombohedral phase

Exp.	*P* (GPa)	$Q(0001)$	$Q(10\bar{1}1)$	$Q(01\bar{1}2)$	$Q(10\bar{1}4)$	$Q(11\bar{2}0)$
$(Mg_{0.08}Fe_{0.88})O$	18.7	0.0049(2)	0.00980(7)	0.00444(2)	0.0085(1)	0.00897(6)
	27.4	0.0154(3)	0.0184(1)	0.00644(3)	0.0160(1)	0.01442(8)
	36.6	0.0177(3)	0.01841(9)	0.00596(3)	0.0171(2)	0.01454(7)
$Fe_{0.94}O$	18.8	0.0078(3)	0.0151(1)	0.00404(3)	0.0138(2)	0.0123(1)
	24.9	0.0152(2)	0.01504(5)	0.00417(2)	0.01533(9)	0.01385(5)
	36.2	0.0199(3)	0.0170(1)	0.00500(3)	0.0280(2)	0.0159(1)

18.8 GPa in cubic $Fe_{0.94}O$, which corresponds to increasing compression, as expected. Because elastic constants of rhombohedral FeO are unknown, values for the parameter $Q(hkl)$ are instead listed for five crystallographic directions: $[0001]_r$, $\langle 10\bar{1}1\rangle_r$, $\langle 01\bar{1}2\rangle_r$, $\langle 10\bar{1}4\rangle_r$, and $\langle 11\bar{2}0\rangle_r$ (Table 2). The $Q(hkl)$ values increase with pressure, indicating increasing elastic strain with pressure, as expected. After decompression back to 1.8 GPa with the $(Mg_{0.08}Fe_{0.88})O$ sample, differential stress changed to −0.01 GPa, nearly the starting value as anticipated for elastic strain. No image was taken near ambient pressure following decompression for $Fe_{0.94}O$ because the beam shut off.

Texture

The three-dimensional orientation distribution that describes the orientations of crystals in a polycrystalline sample may be displayed in two-dimensional pole figures (PFs) or inverse pole figures (IPFs). Although PFs, which describe lattice plane poles relative to sample coordinates, are somewhat more intuitive to read than IPFs, the IPFs display the orientation of the sample symmetry axis (in this case, the compression direction) relative to crystal coordinates and thus are more efficient to represent texture information for axially symmetric textures. Here, we show both and provide instructions on how to interpret each. Both are represented in equal area projection.

Pole figures and cubic texture

Some PFs showing preferred orientation in the cubic phase of $Fe_{0.94}O$ at 15 GPa are presented in Fig. 4 (top row). Contour lines separate areas with different pole densities. Angles η in the PFs with the highest pole densities,

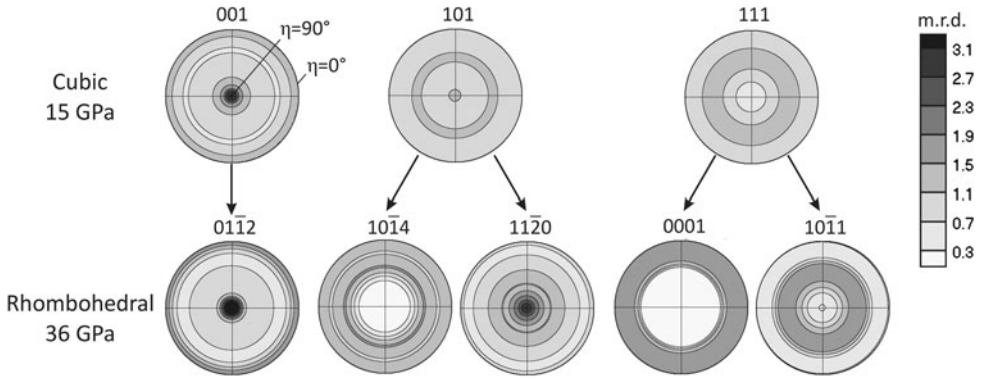

Fig. 4 Pole figures showing texture of cubic $Fe_{0.94}O$ at 15 GPa and room temperature (*top row*) and at 36 GPa and room temperature (*bottom row*). The crystallographic lattice plane normals being viewed are indicated above each pole figure. The compression direction ($\eta = 90°$) lies in the center of each pole figure while the axis perpendicular to the compression direction ($\eta = 0°$) lies in the peripheral. An m.r.d = 1 indicates no preferred orientation is present. A value with an m.r.d = 3 indicates that the crystal face being viewed is three times more likely to align in that direction than if the crystals were randomly oriented. Equal area projection

measured in multiples of random distribution (m.r.d), directly correlate with angles of maximum intensity in the unrolled diffraction pattern (Fig. 3b) for the corresponding peak *hkl*. A PF with m.r.d = 1 shows random orientation while a pole figure with a maximum m.r.d = 3 has crystals that are three times more likely found in that orientation. The compression direction is in the center of each pole figure (at $\eta = 90°$).

The 001_c PF (Fig. 4) for $Fe_{0.94}O$ has two maxima: one located in the center of the PF, and a weaker concentration at $\eta = 0°$; 101_c has two concentrations, one in the compression direction, and another as a girdle at $\eta = 45°$; 111_c has only a single concentration at $\eta = 37.5°$. This is consistent with cubic symmetry. Thus, $\{001\}_c$ planes in cubic $Fe_{0.94}O$ are preferentially aligned perpendicular to the compression direction at pressure. The same was true for $(Mg_{0.08}Fe_{0.88})$. Initially, both samples were nearly randomly oriented and developed the texture shown in Fig. 4 upon compression in the DAC (texture evolution is discussed in greater detail below).

Near 19 GPa, the 111_c, and the 220_c diffraction peaks in the cubic phase split, whereas the 200_c peak did not (Fig. 3b), indicating the lowering of crystal symmetry from cubic-to-rhombohedral. In other words, the $\{111\}_c$ planes are no longer symmetrically equivalent to each other and neither are the $\{101\}_c$ planes; however, $\{001\}_c$ remain equivalent and become $\{01\bar{1}2\}_r$.

Pole figures and rhombohedral texture

PFs in Fig. 4 (bottom row) show that the $\{01\bar{1}2\}_r$ lattice planes of the rhombohedral phase remain preferentially oriented perpendicular to the compression direction. The $\{101\}_c$ planes give rise to two families of rhombohedral planes $\{10\bar{1}4\}_r$ and $\{11\bar{2}0\}_r$, and the $\{111\}_c$ planes, to $(0001)_r$ and $\{10\bar{1}1\}_r$. While the parent $\{101\}_c$ planes do not strongly align perpendicular or parallel to the compression direction, one of its daughters, $\{11\bar{2}0\}_r$, orients perpendicular to the compression direction, and the other, $\{10\bar{1}4\}_r$, aligns at a lower angle to the compression direction. A similar case of variant selection occurs for $\{111\}_c$, with $\{10\bar{1}1\}_r$ orienting more closely perpendicular to the compression direction than $(0001)_r$.

Inverse pole figures and textural evolution

To help illustrate how to read IPFs, two stereographs of equal area projection depict the orientation of a single crystal in the cubic (Fig. 5a) and the rhombohedral (Fig. 5b) reference frames. Labels denote the location at which (*hkl*) poles and [*uvw*] directions would intersect a hemisphere placed above the crystal (represented by the stereographs). Note that the poles perpendicular to planes $(10\bar{1}1)_r$ and $(10\bar{1}4)_r$ are no longer parallel to vectors $[10\bar{1}1]_r$ and $[10\bar{1}4]_r$, respectively, in the rhombohedral phase. Except in the case of cubic symmetry, it is rare for lattice plane normals (*hkl*) to coincide with the directions of the same indices such that $[u = h, v = k, w = l]$.

Figure 6 shows IPFs for the compression direction (top) and for an axis perpendicular to the compression direction (bottom). The first set of IPFs in Fig. 6a, b show preferred orientation of cubic $(Mg_{0.08}Fe_{0.88})O$ as viewed down the $[001]_c$ lattice vector. In the second set of IPFs (Fig. 6c, d), the projection of the cubic texture has been rotated first around $[1\bar{1}0]_c$ by 54.7° clockwise (if looking in the $[1\bar{1}0]_c$ direction) to bring $(111)_c$ into the center, then around $[111]_c$ by 150° clockwise. We show cubic texture as viewed down $[111]_c$ to show the relationship between cubic (Fig. 6c, d) and rhombohedral texture (Fig. 6e, f). Maxima seen in (a) and (c) are equal but rotated, but texture maxima in (c) and (e) differ. Specifically, the pole densities at $\{10\bar{1}4\}_r$ and $\{11\bar{2}0\}_r$ are no longer equal, and

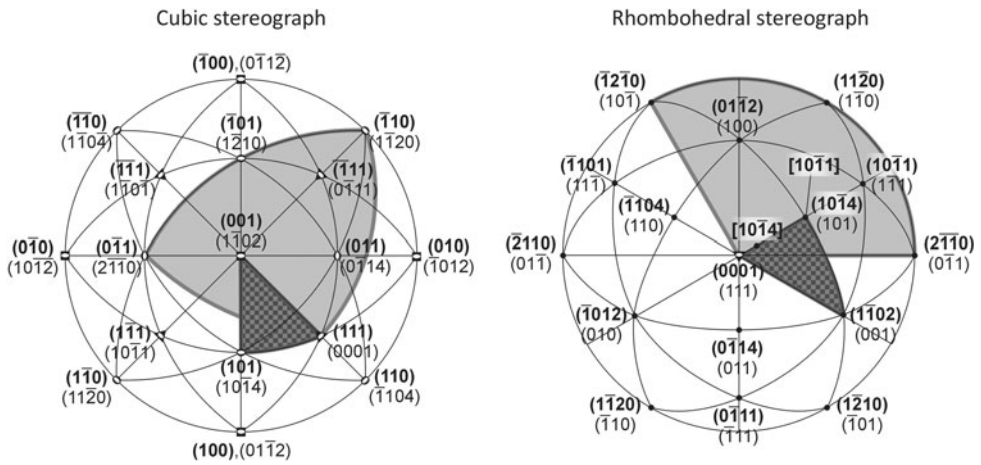

Fig. 5 Stereonets for the cubic reference frame (*left*) and the rhombohedral reference frame (*right*). *Bolded* coordinates pertain to the stereonet they are located in, and equivalent coordinates are shown in *plain text*. *Squares* denote poles with fourfold symmetry, *triangles* denote threefold symmetry, *black ovals*, twofold symmetry, and *white ovals*, inversion points. The area covered by the cubic IPF is denoted with *dotted* texture while the area covered by the rhombohedral IPF is shown in *lighter gray*. Indices for lattice plane normals are in rounded parentheses, those for lattice directions in *square brackets*. Equal area projections

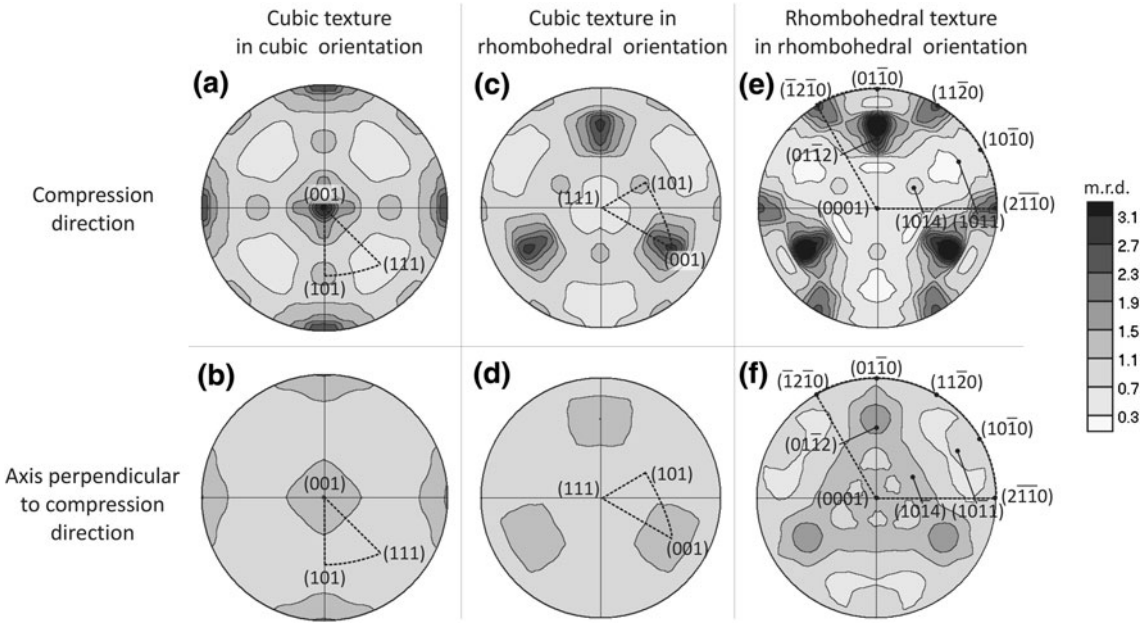

Fig. 6 Full inverse pole figures depicting the crystallographic relationship between cubic $(Mg_{0.08}Fe_{0.88})O$ at 14 GPa and rhombohedral $(Mg_{0.08}Fe_{0.88})O$ at 27 GPa. Areas inside the *dotted lines* correspond to areas highlighted in Fig. 5 and slices shown in Fig. 7. Important crystallographic directions are labeled. Evidence of variant selection is seen by comparing **c**–**e** and **d**–**f**. Directions with equal m.r.d values in **c**, for example, no longer have equal values in **e**. Equal area projections

neither are the pole densities at $(0001)_r$ and $\{10\bar{1}1\}_r$. IPFs for the axis perpendicular to the compression direction (Fig. 6b, d, f) show the same trend: $\{10\bar{1}4\}_r$ and $\{11\bar{2}0\}_r$ no longer have the same pole densities in (f), and neither do $(0001)_r$ and $\{10\bar{1}1\}_r$.

The entire IPF (360°) is usually not shown as crystal symmetry makes it redundant. It is standard to instead show only the areas contained within the dotted lines in Fig. 6, and this is what we display in Fig. 7. The starting textures in Fig. 7 are weak; however, there is already a maximum of 1.84 m.r.d at 0.2 GPa at $\{001\}_c$ in $Fe_{0.94}O$ likely due to the fact that differential stress was already −0.42 at 0.2 GPa. As mentioned earlier, some stress may have been applied to the sample when closing the DAC. Texture sharpness increased with pressure in the cubic phase (here "texture sharpness" refers to the maximum

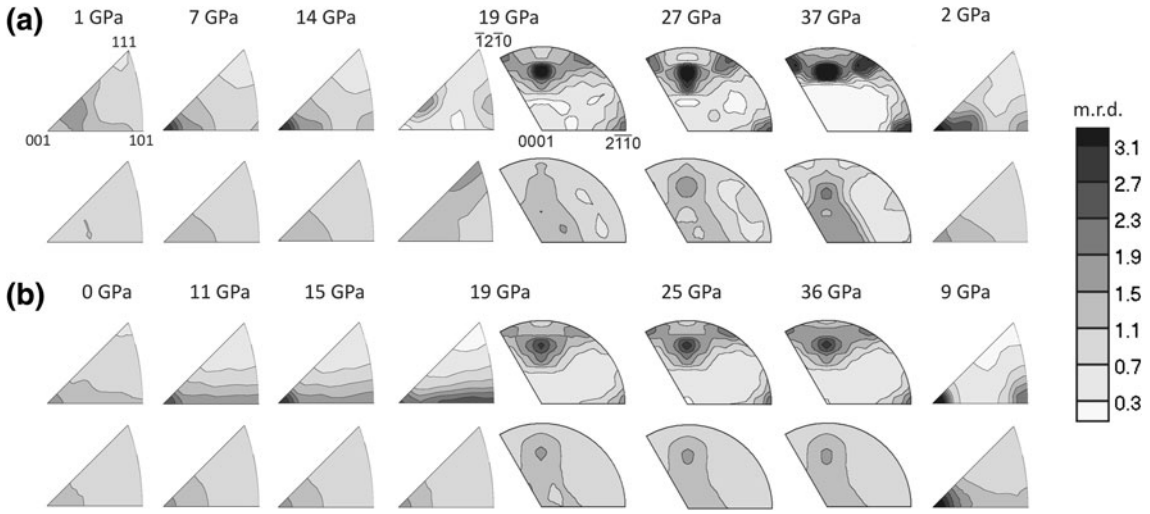

Fig. 7 **a** IPFs showing textural evolution of $(Mg_{0.08}Fe_{0.88})O$ up to 36.6 GPa through the phase transition from cubic-to-rhombohedral and returning to cubic upon decompression; compression direction shown in *top row*, and axis perpendicular to the compression direction shown in *second row*. **b** Texture evolution of $Fe_{0.94}O$ up to 36.2 GPa. Texture sharpness is measured in multiples of random distribution (m.r.d). Equal area projections

pole density in the PFs and IPFs) at $\{001\}_c$ from 1.80 to 3.28 m.r.d in $(Mg_{0.08}Fe_{0.88})O$ and from 1.84 to 3.15 m.r.d in $Fe_{0.94}O$; it also increased at $\{101\}_c$ in $(Mg_{0.08}Fe_{0.88})O$.

Near the phase transition at 19 GPa, both the cubic and the rhombohedral phase were present. The maximum at $\{001\}_c$ in the cubic phase disappeared, and a maximum at $\{01\bar{1}2\}_r$ appeared in the rhombohedral phase. In the rhombohedral phase, texture sharpness increased with pressure, much more so in the $(Mg_{0.08}Fe_{0.88})O$ sample (from 3.94 to 6.48 m.r.d) than the $Fe_{0.94}O$ sample (from 2.82 to 2.90 m.r.d). Pole densities increased specifically at $\{01\bar{1}2\}_r$ and $\{11\bar{2}0\}_r$ in both samples.

Upon decompression back to the cubic phase, the maximum at $\{001\}_c$ returned, but stronger than it was before the phase transition: 4.24 m.r.d in $(Mg_{0.08}Fe_{0.88})O$ and 7.28 m.r.d in $Fe_{0.94}O$. In addition, the secondary maximum at $\{101\}_c$ reappeared in the $(Mg_{0.08}Fe_{0.88})O$ sample and appeared for the first time in the $Fe_{0.94}O$.

Discussion

Texture

Initial texture at 1 and 0 GPa in $(Mg_{0.08}Fe_{0.88})O$ and $Fe_{0.94}O$, respectively, was weak. As we increased pressure in the cubic phase, a maximum pole density in the IPFs (Fig. 7) developed and grew at $\{001\}_c$. Similar results for cubic texture were obtained by Merkel et al. (2002) for MgO, by Tommaseo et al. (2006) for $(Mg_{0.4}Fe_{0.6})O$, $(Mg_{0.25}Fe_{0.75})O$, and $(Mg_{0.1}Fe_{0.9})O$, and by Lin et al. (2009) for $(Mg_{0.83}Fe_{0.17})O$.

At the phase transition, near 19 GPa, the maximum in the cubic phase shifted away from $\{001\}_c$ (Fig. 7). This can be explained by crystals in this orientation transitioning to the rhombohedral phase before crystals in other orientations. This also explains why the maximum at $\{01\bar{1}2\}_r$ developed immediately while the maxima at $\{2\bar{1}\bar{1}0\}_r$ developed later under greater stress. A similar phenomenon of certain crystal orientations transitioning first to a new phase was also observed in the hcp-to-bcc transition in Ti (Lonardelli et al. 2007) and in the bcc-to-hcp transition in Fe (Miyagi et al. 2008).

In the rhombohedral phase, we observed that one daughter of $\{101\}_c$, $\{11\bar{2}0\}_r$, orients perpendicular to the compression direction, and the other, $\{10\bar{1}4\}_r$, aligns at a low angle to the compression direction (Fig. 4). Similarly, one daughter of $\{111\}_c$, $\{10\bar{1}1\}_r$, orients more closely perpendicular to the compression direction than its sibling, $(0001)_r$. This variant selection may be because $\langle 10\bar{1}4\rangle_r$ and $[0001]_r$ are the plastically softer of the two sets of directions. Crystals with their $\{10\bar{1}4\}_r$ and/or $(0001)_r$ planes perpendicular to the compression direction would experience the greatest amount of strain along $\langle 10\bar{1}4\rangle_r$ and/or $[0001]_r$. If $\langle 10\bar{1}4\rangle_r$ and/or $[0001]_r$ were soft directions, it would be more favorable for these crystals to rotate or nucleate such that their $\{11\bar{2}0\}_r$ and/or $\{10\bar{1}1\}_r$ planes are at high angles to the compression direction, thus putting stiffer directions $\langle 11\bar{2}0\rangle_r$ and/or $\langle 10\bar{1}1\rangle_r$ more closely parallel to the compression direction. PFs in Fig. 4 show that it is in fact more likely to find crystals in this orientation. This variant selection is briefly explored with viscoplastic self-consistent modeling below.

Upon decompression back to the cubic phase, the reappearance of the maxima at $\{001\}_c$ and $\{101\}_c$ with a greater texture sharpness than before the phase transition (Fig. 7) is likely due to an increase in texture sharpness in

the rhombohedral phase during subsequent deformation at $\{01\bar{1}2\}_r$ and $\{11\bar{2}0\}_r$, respectively.

Overall, stronger texture developed in the $(Mg_{0.08}Fe_{0.88})O$ sample than in the $Fe_{0.94}O$. Similarly, Tommaseo et al. (2006) observed stronger textures in magnesiowüstite samples with higher magnesium content. Stronger texture in the $(Mg_{0.08}Fe_{0.88})O$ experiment may also be due to high plastic strain, as we will discuss below.

Viscoplastic self-consistent modeling

Both elastic lattice strain and plastic deformation are imposed on the sample during axial shortening in DAC experiments. While elastic strains indicate stress conditions inside the sample chamber and are relatively small, plastic strains are much greater and produce preferred orientation. Texture development in plastically deforming polycrystals can be approached with polycrystal plasticity models that predict slip system activity and lattice rotations under an externally imposed strain (e.g., Kocks et al. 1998). The viscoplastic self-consistent (VPSC) approach for modeling texture ignores elastic strains and considers only plastic deformation (Lebensohn and Tomé 1994). In VPSC simulations, individual grains deform inside a homogenous but anisotropic medium with the same properties as the aggregate average. Deformation (and rotation) of lattice planes inside grains depends on their orientation relative to the compression direction. However, interaction among individual grains is not taken into account. Also, work hardening is not considered here because there are no data for this system.

By comparing textures produced by VPSC simulations with experimental textures, we can estimate slip systems that are active during the experiment. In the simulations, 2,000 grains were compressed to 50 and 70 % axial shortening in 50 and 70 steps, respectively. For the cubic phase, the observed starting texture was nearly random; correspondingly, an initially random orientation distribution was assumed in VPSC. For the rhombohedral phase, both a random starting texture and a cubic starting texture (produced from VPSC) were considered (Fig. 8).

Potential slip systems are well known in B1 structures. In halite, deformation at low temperatures occurs primarily by slip on $\{110\}\langle 1\bar{1}0\rangle_c$ (Carter and Heard 1970; Skrotzki and Haasen 1981), and however, harder systems $\{111\}_c$ and $\{100\}_c$ can also be activated. Deformation in MgO is similar, but much more plastically anisotropic (Paterson and Weaver 1970; Meade and Jeanloz 1988; Foitzik et al. 1989), making $\{111\}_c$ and $\{100\}_c$ less active than they are in halite. Using these same three slip systems, texture evolution of halite and magnesiowüstite was already explored with polycrystal plasticity modeling (e.g., Wenk et al. 1989; Merkel et al. 2002; Lin et al. 2009). Here, we repeat some of these calculations. Relative critical resolved shear stresses (CRSS) for the cubic phase were chosen to be 0.5 for $\{110\}\langle 1\bar{1}0\rangle_c$, 1.5 for $\{111\}\langle 1\bar{1}0\rangle_c$, and 3.0 for $\{100\}\langle 1\bar{1}0\rangle_c$ to obtain a texture maximum at $\{001\}_c$ in the IPF as observed in experiments. As with the experimental orientation distributions, calculated orientation distributions were smoothed and then plotted as IPFs. Textures produced in VPSC simulations (Fig. 8) can be directly compared to experimental textures (Fig. 7).

A primarily active $\{110\}\langle 1\bar{1}0\rangle_c$ slip system supports the idea that crystals with their $\{001\}_c$ planes at high angles to the compression direction, and thus according to Schmid's Law optimally oriented for $\{110\}\langle 1\bar{1}0\rangle_c$ slip, are the first to transition to the rhombohedral phase as mentioned earlier. Crystals in this orientation do not rotate due to two pairs of slip systems (e.g., $(110)[1\bar{1}0]_c$ and $(1\bar{1}0)[110]_c$) that are at equal angles to the compression direction, making them equally active in opposite directions, hence canceling out the rotation of each other. The other slip systems in $\{110\}\langle 1\bar{1}0\rangle_c$ have a Schmidt factor of zero and also do not cause rotation. Meanwhile, crystals in other orientations experience less strain as they rotate toward the preferred orientation at a rate that depends on their individual orientations.

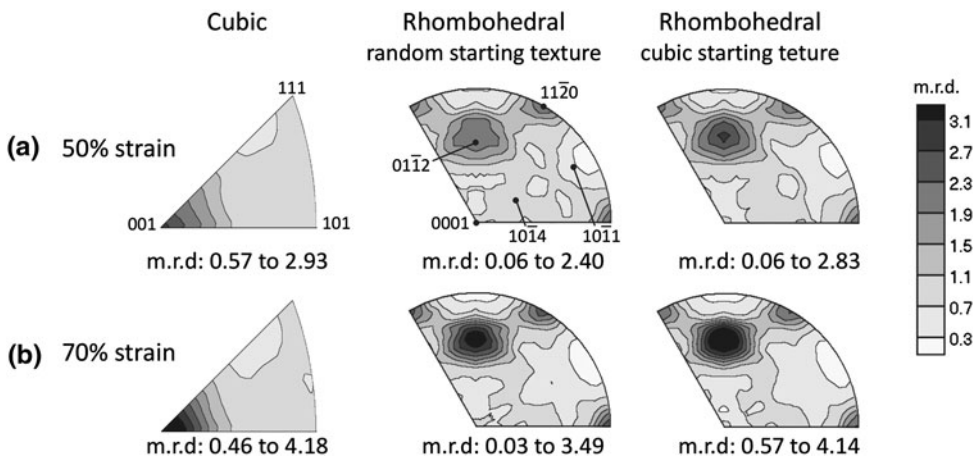

Fig. 8 IPFs calculated at **a** 50 % and **b** 70 % axial shortening produced with VPSC for the cubic and rhombohedral phases of (Mg,Fe)O. Comparison of the effect of random and starting texture on the final texture is shown for rhombohedral (Mg,Fe)O. Simulations with stress exponent $n = 12$ produced the closest match to experiment. Equal area projections

Rhombohedral slip systems

Two sets of VPSC simulations were performed for the rhombohedral phase, one with a starting texture of 5,000 crystals in random orientation, and one with 2,000 crystals in the preferred cubic orientation. The starting cubic texture is the same texture obtained from the VPSC simulations for the cubic phase described above. For both sets of simulations, daughter slip systems in the rhombohedral phase $\{11\bar{2}0\}\langle\bar{1}101\rangle_r$ and $\{10\bar{1}4\}\langle1\bar{2}10\rangle_r$ were initially assigned the same CRSS of 0.5 as their parent, $\{110\}\langle1\bar{1}0\rangle_c$. Similarly, $(0001)\langle11\bar{2}0\rangle_r$, $\{10\bar{1}1\}\langle\bar{1}2\bar{1}0\rangle_r$, and $\{10\bar{1}1\}\langle1\bar{1}0\bar{1}\rangle_r$ were initially given a CRSS of 1.5, and $\{01\bar{1}2\}\langle21\bar{1}0\rangle_r$ and $\{01\bar{1}2\}\langle01\bar{1}\bar{1}\rangle_r$, 3.0. CRSS were then varied from these initial values to find the closest match to experimental rhombohedral textures.

For both starting textures, pole density maxima at $\{01\bar{1}2\}_r$ appeared with the starting CRSS mentioned above, producing similar IPFs as shown in Fig. 6c, d. The $\{10\bar{1}1\}\langle\bar{1}2\bar{1}0\rangle_r$ daughter of $\{111\}\langle1\bar{1}0\rangle_c$ was then preferentially activated by reducing the CRSS from 1.5 (as it was in the cubic phase) to 1, resulting in a secondary maximum at $\{11\bar{2}0\}_r$ (Fig. 8) as seen in the experimental IPFs. Meanwhile, sibling slip systems $(0001)\langle11\bar{2}0\rangle_r$ and $\{10\bar{1}1\}\langle01\bar{1}\bar{1}\rangle_r$ retained the same CRSS they had in the cubic phase. Because $\{10\bar{1}1\}\langle\bar{1}2\bar{1}0\rangle_r$ is the only slip system with a CRSS that differs between the cubic phase and the rhombohedral phase, it is responsible for the variant selection that aligns $\{11\bar{2}0\}_r$ more closely perpendicular to the compression direction rather than its sibling $\{10\bar{1}4\}_r$.

The VPSC model with initial random texture shows nearly equivalent pole densities at $\{11\bar{2}0\}_r$ and at $\{01\bar{1}2\}_r$, whereas the model with cubic starting texture shows a higher m.r.d at $\{01\bar{1}2\}_r$, which is also true of the experimental texture shown in Fig. 7. A closer match between VPSC results with cubic starting texture and experiment suggests that preferred orientation was not randomized by the phase transition. Instead, crystallographic orientations continued to evolve through the rhombohedral distortion, further supporting the theory that $\{001\}_c$-oriented crystals transition to the rhombohedral phase first.

Strain and strain rate sensitivity

We find a best match to experiments when VPSC simulations are carried out to 50–70 % strain. For comparison, Lin et al. (2009) found a best match between experiment and VPSC with 100 % strain, and Merkel et al. (2002) found a best match with 50–100 % strain, depending on applied pressure in the DAC. While 50 % strain accurately reproduces texture sharpness for the experiment performed with $Fe_{0.94}O$, 70 % strain provides a closer match to data for $(Mg_{0.08}Fe_{0.88})O$. Because we cannot reliably measure the total strain on the sample during the experiment, our best estimate for strain, based on VPSC simulations, is 50 and 70 % at 36 GPa in $Fe_{0.94}O$ and $(Mg_{0.08}Fe_{0.88})O$, respectively. The difference in strain may be due to experimental techniques: while pressure was applied more smoothly to the $Fe_{0.94}O$ sample using a remote-controlled gas membrane, it was incrementally and suddenly applied to the $(Mg_{0.08}Fe_{0.88})O$ using a lever arm. As stated above, it may also be due to the difference in elasticity in the two compositions. The plastic strain that is achieved in DAC experiments depends greatly on gasket materials.

Visco-plastic deformation is often described with a flow law $\dot{\varepsilon} = A\sigma^n$, where $\dot{\varepsilon}$ is the strain rate (s^{-1}), A is a constant (MPa^{-n} s^{-1}), σ is differential stress (MPa), and n is the stress exponent, that is the strain rate sensitivity to stress (e.g., Kirby and Kronenberg 1987). Low values of stress exponent n (i.e. $n \leq 3$) typically correspond to higher diffusion activity (higher temperatures) causing strain to become distributed over many slip systems (e.g., Kocks et al. 1998). As n increases, diffusion activity decreases and strain becomes concentrated on fewer slip systems. The best match to experimental data for both cubic and rhombohedral was found with $n = 12$, which is reasonable for deformation at ambient temperature with little diffusion.

Slip system activities that provided the closest match to experimental textures for $n = 12$ are summarized in Table 3. For $n = 12$, $\{110\}\langle1\bar{1}0\rangle_c$ is the most active slip system in the cubic phase with CRSS = 0.5; it comprises 99 % of slip active at 0 % strain and 100 % of slip activity at 50 and 70 % strain. In the rhombohedral phase, for $n = 12$, slip systems $\{10\bar{1}4\}\langle1\bar{2}\bar{1}0\rangle_r$, and $\{11\bar{2}0\}\langle\bar{1}101\rangle_r$ have CRSS = 0.5 and each makes up 45 % of slip system activity at 0 % strain and 48 % at 50 % and 70 % strain with a random starting texture. For a cubic starting texture, each comprises 46 % slip system activity at 0 % strain, 48 % at 50 % strain, and 49 % at 70 % strain. Slip system $\{10\bar{1}1\}\langle\bar{1}210\rangle_r$ has CRSS = 1.0 and is responsible for nearly all remaining activity in the rhombohedral phase. Rhombohedral slip systems $(0001)\langle11\bar{2}0\rangle_r$ and $\{10\bar{1}1\}\langle1\bar{1}0\bar{1}\rangle_r$ showed negligible activity and are not listed in Table 3. Cubic slip system $\{100\}\langle1\bar{1}0\rangle_c$ and its daughter rhombohedral slip systems $(01\bar{1}2)\langle2\bar{1}\bar{1}0\rangle_r$ and $\{01\bar{1}2\}\langle01\bar{1}\bar{1}\rangle_r$ showed no activity and so are also not listed in Table 3.

There are some differences between texture observed in experiments and texture obtained from VPSC modeling. For example, the experimental texture in the cubic phase for $(Mg_{0.08}Fe_{0.88})O$ and for $Fe_{0.94}O$ after decompression shows a secondary maximum at $\{101\}_c$ (Fig. 7) that is absent from the VPSC-obtained cubic texture (Fig. 8). The secondary maxima at $\{101\}_c$ appears in VPSC models for a lower stress exponent (e.g., $n = 9$), or equivalently, slightly

Table 3 Activities for the slip systems of cubic (Mg,Fe)O and rhombohedral (Mg,Fe)O at 0, 50, and 70 % strain as calculated with VPSC

Symmetry	Cubic		Rhombohedral					
Slip system	$\{110\}\langle 1\bar{1}0\rangle$	$(111)\langle 1\bar{1}0\rangle$	$\{10\bar{1}4\}\langle 1\bar{2}10\rangle$		$\{11\bar{2}0\}\langle \bar{1}101\rangle$		$\{10\bar{1}1\}\langle \bar{1}2\bar{1}0\rangle$	
CRSS	0.5	1.5	0.5		0.5		1.0	
	Activity (%)	Activity (%)	Activity (%)		Activity (%)		Activity (%)	
Starting texture	Random	Random	Random	Cubic	Random	Cubic	Random	Cubic
At 0 % strain	99	1	45	46	45	46	9	8
At 50 % strain	100	0	48	48	48	48	4	3
At 70 % strain	100	0	48	49	48	49	3	3

Rhombohedral activities are shown for both a starting random texture and a starting cubic texture. CRSS used provide the closest match to experimental textures. Rhombohedral slip systems $(0001)\langle 11\bar{2}0\rangle_r$ and $\{10\bar{1}1\}\langle 1\bar{1}0\bar{1}\rangle_r$ were included in calculations but showed negligible activity and so are not listed. Cubic slip system $\{100\}\langle 1\bar{1}0\rangle_c$ and rhombohedral slip systems $\{01\bar{1}2\}\langle 2\bar{1}\bar{1}0\rangle_r$ and $\{01\bar{1}2\}\langle 01\bar{1}\bar{1}\rangle_r$ were also used in calculations but showed no activity, so are also not listed. Activities and CRSS for 50 and 70 % strain listed here correspond to IPFs shown in Fig. 8

increased activity of $\{111\}\langle 1\bar{1}0\rangle_c$. In this study, we have chosen to simplify deformation by describing it with one slip system. A few differences between experimental and modeled texture also exist for the rhombohedral phase: positions of minima and shape of the maximum differ between the experimental IPFs and VPSC-generated IPFs. These differences are likely beyond the resolution of the orientation distribution in MAUD (15° × 15° × 15°) and are negligible.

Conclusions

We compressed two powdered samples, $(Mg_{0.08}Fe_{0.88})O$ magnesiowüstite and $Fe_{0.94}O$ wüstite, non-hydrostatically up to 36 GPa at ambient temperature in the DAC. Experiments were performed in radial geometry in order to observe textural evolution as a function of pressure. A pole density maximum developed in the center of the 001_c pole figures for both $(Mg_{0.08}Fe_{0.88})O$ and $Fe_{0.94}O$ (Fig. 4) upon compression and texture sharpness increased as pressure increased. Near 19 GPa, the 111_c and 220_c peaks split, while 200_c did not, in both experiments, indicating a transition to the rhombohedral phase. Variant selection aligned $\{11\bar{2}0\}_r$, a daughter of $\{101\}_c$, and $\{10\bar{1}1\}_r$, a daughter of $\{111\}_c$, more closely perpendicular to the compression direction. This may be due to elastically softer crystal directions aligning perpendicular to the compression direction in a more thermodynamically stable arrangement. Unfortunately, the elastic constants of Fe-rich members of the MgO-FeO solid-solution series are not yet known to confirm this. On the other hand, the variant selection may be due to progressive deformation of the rhombohedral phase with different slip system activities. Using polycrystal plasticity simulations, we found deformation in the cubic phase of solid-solution (Mg,Fe)O to be due mostly to slip on $\{110\}\langle 1\bar{1}0\rangle_c$ as previously found for other B1 structures. In the rhombohedral phase, slip system activity changed slightly with one of the daughters of $\{111\}\langle 1\bar{1}0\rangle_c$, $\{10\bar{1}1\}\langle \bar{1}2\bar{1}0\rangle_r$ (inactive in the cubic phase), becoming active.

Interestingly, texture near the transition pressure suggests that crystals in the cubic phase with their $\{001\}_c$ planes facing the compression direction are preferentially oriented to transform to the rhombohedral phase first. Orientations that developed and strengthened in the rhombohedral phase remained after decompression back to the cubic phase. Upon decompression, a texture similar to the cubic one before the phase transition was observed, suggesting a memory during this displacive transition.

Acknowledgments Pamela Kaercher is grateful for partial support from the Francis J. Turner Fellowship. We also thank the Carnegie/Department of Energy Alliance Center (CDAC) and the National Science Foundation (EAR-0836402) for financial support and the Advanced Light Source of Lawrence Berkeley National Laboratory for the use of beamline 12.2.2. Samples were provided by Yingwei Fei via Ho-kwang Mao, and Steven Jacobsen. We appreciate assistance with the experiments from Hauke Marquardt, Sebastian Merkel, and Jason Knight. Carlos Tomé developed the viscoplastic self-consistent code used here to determine slip systems. We are appreciative to constructive comments from reviewers.

References

Antonangeli D, Siebert J, Aracne C, Farber D, Bosak A, Hoesch M, Krisch M, Ryerson F, Fiquet G, Badro J (2011) Spin crossover in ferropericlase at high pressure: a seismologically transparent transition? Science 331:64–67

Badro J, Struzhkin V, Shu J, Hemley R, Mao HK (1999) Magnetism in FeO at megabar pressures from X-ray emission spectroscopy. Phys Rev Lett 83(20):4101–4104

Badro J, Guillaume F, François G, Rueff JP, Struzhkin V, Vankó G, Monaco G (2003) Iron partitioning in earth's mantle: toward a deep lower mantle discontinuity. Science 300:789–791

Bonczar L, Graham E (1982) The pressure and temperature dependence of the elastic constants of polycrystal magnesiowustite. J Geophys Res 87(B2):1061–1078

Carter N, Heard H (1970) Temperature and rate dependent deformation of halite. Am J Sci 269:193–249

Cohen R, Mazin I, Isaak D (1997) Magnetic collapse in transition metal oxides at high pressure: implications for the earth. Science 275(654). doi:10.1126/science.275.5300.654

Crowhurst J, Brown J, Goncharov A, Jacobsen S (2008) Elasticity of (Mg, Fe)O through the spin transition of iron in the lower mantle. Science 319:451–453

Ding Y, Xu J, Prewitt C, Hemley R, Mao HK, Cowan J, Zhang J, Qian J, Vogel S, Lokshin K, Zhao Y (2005) Variable pressure-temperature neutron diffraction of wüstite (Fe_{1-x} O): absence of long-range magnetic order to 20 GPa. Appl Phys Lett 86:052505

Dubrovinsky L, Dubrovinskaia N, Saxena S, LiBehan T (2000) X-ray diffraction under non-hydrostatic conditions in experiments with diamond anvil cell: wustite (FeO) as an example. Mat Sci Eng A288:187–190

Duffy T, Hemley R, Mao HK (1995) Equation of state and shear strength at multimegabar pressures: magnesium oxide to 227 GPa. Phys Rev Lett 74(8):1371–1374

Fei Y (1996) Crystal chemistry of FeO at high pressure and temperature. Geochem Soc 5:243–254

Fei Y, Mao HK (1994) In situ determination of the NiAs phase of FeO at high pressure and temperature. Science 266(5191):1678–1680

Fei Y, Zhang L, Corgne A, Watson H, Ricolleau A, Meng Y, Prakapenka V (2007) Spin transition and equations of state of (Mg, Fe)O solid solutions. Geophys Res Lett. doi:10.1029/2007GL030712

Foitzik A, Skrotzki W, Haasen P (1989) Correlation between microstructure, dislocation dissociation and plastic anisotropy in ionic crystals. Mat Sci Eng A113:399–407

Gramsch S, Cohen R, Savrasov S (2003) Structure, metal-insulator transitions, and magnetic properties of FeO at high pressures. Am Mineral 88:257–261

Hammersley A, Svensson S, Hanfland M, Fitch A, Häusermann D (1996) Two-dimensional detector software: from real detector to idealised image two-theta scan. High Press Res 14:235–248

Hazen R (1981) Systematic variation of bulk modulus of wüstite with stoichiometry. Year Book, Carnegie Institute of Washington, Washington, vol 80, pp 277–280

Irifune T, Shinmei T, McCammon C, Miyajima N, Rubie D, Frost D (2010) Iron partitioning and density changes in pyrolite in Earth's lower mantle. Science 327:193–195

Jackson I, Ringwood A (1981) High-pressure polymorphism of the iron oxides. Geophys J R Astron Soc 64:767–783

Jackson I, Khanna S, Revcolevschi A, Berthon J (1990) Elasticity, shear-mode softening and high-pressure polymorphism of wustite ($Fe_{1-x}O$). J Geophys Res 21:671–685

Jacobsen S, Spetzler H, Reichmann H, Smyth J (2004) Shear waves in the diamond-anvil cell reveal pressure-induced instability in (Mg, Fe)O. Proc Natl Acad Sci USA 101(16):5867–5871

Jeanloz R, Sato-Sorensen Y (1986) Hydrostatic compression of $Fe_{1-x}O$ wüstite. J Geophys Res 91:4665–4672

Jeanloz R, Thompson A (1983) Phase transitions and mantle discontinuities. Rev Geophys 21:51–74

Kantor A, Jacobsen S, Kantor I, Dubrovinsky L, McCammon C, Reichmann H, Goncharenko I (2004a) Pressure-induced magnetization in FeO: evidence from elasticity and Mössbauer spectroscopy. Phys Rev Lett. doi:10.1103/93.215502

Kantor I, McCammon C, Dubrovinsky L (2004b) Mössbauer spectroscopic study of pressure-induced magnetisation in wüstite (FeO). J Alloys Compd 376:5–8

Kantor I, Dubrovinsky L, McCammon C, Kantor A, Pascarelli S, Aquilanti G, Crichton W, Mattesini M, Ahuja R, Almeida J, Urusov V (2006) Pressure-induced phase transition in $Mg_{0.8}Fe_{0.2}O$ ferropericlase. Phys Chem Miner 33:35–44

Kantor I, Dubrovinsky L, McCammon C, Dubrvinskaia N, Goncharenko I, Kantor A, Kuznetsov A, Crichton W (2007) FeO and MnO high-pressure phase diagrams: relations between structural and magnetic properties. Phase Transitions 80:1151–1163

Kirby S, Kronenberg A (1987) Rheology of the lithosphere; selected topics. Rev Geophys 25(6):1219–1244

Koči L, Vitos L, Ahuja R (2007) Ab initio calculations of the elastic properties of ferropericlase $Mg_{1-x}Fe_xO$ ($x < 0.25$). Phys Earth Planet Interiors 164:177–185

Kocks U, Tomé C, Wenk HR (1998) Texture and anisotropy: preferred orientations in polycrystals and their effect on materials properties. Cambridge University Press, Cambridge, pp 564–567

Kondo T, Ohtani E, Hirao N, Yagi T, Kikegawa T (2004) Phase transitions of (Mg, Fe)O at megabar pressures. Phys Earth Planet Interiors 143–144:201–213

Lebensohn R, Tomé C (1994) A self-consistent viscoplastic model: prediction of rolling textures of anisotropic polycrystals. Mat Sci Eng A175:71–82

Lin JF, Heinz D, Mao HK, Hemley R, Devine J, Li J, Shen G (2003) Stability of magnesiowüstite in Earth's lower mantle. Proc Natl Acad Sci USA 100:4405–4408

Lin JF, Struzhkin V, Jacobsen S, Hu M, Chow P, Kung J, Liu H, Mao HK, Hemley R (2005a) Spin transition of iron in magnesiowustite in the Earth's lower mantle. Nature 436:377–380

Lin JF, Struzhkin V, Jacobsen S, Shen G, Prakapenka V, Mao HK, Hemley R (2005b) X-ray emission spectroscopy with a laser-heated diamond anvil cell: a new experimental probe of the spin state of iron in the Earth's interior. J Synchrotron Radiat 12:637–641

Lin JF, Wenk HR, Voltolini M, Speziale S, Shu J, Duffy T (2009) Deformation of lower-mantle ferropericlase (Mg, Fe)O across the electronic spin transition. Phys Chem Miner 36(10):585–592

Lonardelli I, Gey N, Wenk HR, Humbert M, Vogel S, Lutterotti L (2007) In situ observation of texture evolution during $\alpha \rightarrow \beta$ and $\beta \rightarrow \alpha$ phase transformations in titanium alloys investigated by neutron diffraction. Acta Mater 55:5718–5727

Lutterotti L, Scardi P (1990) Simultaneous structure and size-strain refinement by the Rietveld method. J Appl Phys 23:246–252

Lutterotti L, Matthies S, Wenk HR (1997) Combined texture and structure analysis of deformed limestone from time-of-flight neutron diffraction spectra. J Appl Phys 81(2):594–600

Mao HK, Shu J, Fei Y, Hu J, Hemley R (1996) The wustite enigma. Phys Earth Planet Interiors 96:135–145

Mao W, Shu J, Fei Y, Hu J, Hemley R, Mao HK (2002) Displacive transition in magnesiowustite. J Phys: Condens Matter 14:11349–11354

Mao Z, Lin JF, Liu J, Prakapenka V (2011) Thermal equation of state of lower-mantle ferropericlase across the spin crossover. Geophys Res Lett 38:L23308

Marquardt H, Speziale S, Reichmann H, Frost D, Schilling F, Garnero E (2009) Elastic shear anisotropy of ferropericlase in earth's lower mantle. Science 324. doi:10.1126/science.1169365

Matthies S, Vinel G (1982) An example demonstrating a new reproduction method of the ODF of texturized samples from reduced pole figures. Phys Status Solidi B 112:K115–K120

Matthies S, Priesmeyer H, Daymond M (2001) On the diffractive determination of single-crystal elastic constants using polycrystalline samples. J Appl Cryst 34:585–601

Mazin I, Fei Y, Downs R, Cohen R (1998) Possible polytypism in FeO at high pressures. Am Mineral 83:451–457

Meade C, Jeanloz R (1988) Yield strength of MgO to 40 GPa. J Geophys Res 93:3261–3269

Menendez-Proupin E, Singh A (2007) Ab initio calculations of elastic properties of compressed Pt. Phys Rev B. doi:10.1103/76.054117

Merkel S, Wenk HR, Shu J, Shen G, Gillet P, Mao HK, Hemley R (2002) Deformation of polycrystalline MgO at pressures of the lower mantle. J Geophys Res. doi:10.1029/2001JB000920

Merkel S, Tomé C, Wenk HR (2009) Modeling analysis of the influence of plasticity on high pressure deformation of hcp-Co. Phys Rev B. doi:10.1103/79.064110

Miyagi L, Kunz M, Knight J, Nasiatka J, Voltolini M, Wenk HR (2008) In situ phase transformation and deformation of iron at high pressure and temperature. J Appl Phys. doi:10.1063/1.3008035

Murakami M, Hirose K, Ono S, Tsuchiya T, Isshiki M, Watanuki T (2004) High pressure and high temperature phase transitions of FeO. Phys Earth Planet Interiors 146:273–282

Ohta K, Cohen R, Hirose K, Haule K, Shimizu K, Ohishi Y (2012) Experimental and theoretical evidence for pressure-induced metallization in FeO with rock-salt-type structure. Phys Rev Lett 108:026403

Ozawa H, Takahashi F, Hirose K, Ohishi Y, Hirao N (2011) Phase transition of FeO and stratification in Earth's outer core. Science 334:792–794. doi:10.1126/science.1208265

Pasternak M, Taylor R, Jeanloz R, Li X, Nguyen J, McCammon C (1997) High pressure collapse of magnetism in $Fe_{0.94}O$: Mössbauer spectroscopy beyond 100 GPa. Phys Rev Lett 79(25):5046–5049

Paterson M, Weaver C (1970) Deformation of polycrystalline MgO under pressure. J Am Ceram Soc 53:463–471

Rietveld H (1969) A profile refinement method for nuclear and magnetic structures. J Appl Cryst 2:65–71

Shim SH, Duffy T, Kenichi T (2002) Equation of state of gold and its application to the phase boundaries near 660 km depth in Earth's mantle. Earth Planet Sci Lett 203:729–739

Shu J, Mao HK, Hu J, Fei Y, Hemley R (1998) Single-crystal X-ray diffraction of wustite to 30 GPa hydrostatic pressure. N Jb Miner Abh 172:309–323

Singh A, Mao HK, Shu J, Hemley R (1998) Estimation of single-crystal elastic moduli from polycrystalline X-ray diffraction at high pressure: application to FeO and iron. Phys Rev Lett 80(10):2157–2160

Skrotzki W, Haasen P (1981) Hardening mechanisms of ionic crystals on (110) and (100) slip planes. J Phys (Paris) 42(6):3119–3148

Speziale S, Milner A, Lee V, Clark S, Pasternak M, Jeanloz R (2005) Iron spin transition in earth's mantle. Proc Natl Acad Sci USA 102(50):17918–17922

Speziale S, Lee V, Clark S, Lin J, Pasternak M, Jeanloz R (2007) Effects of Fe spin transition on the elasticity of (Mg, Fe)O magnesiowüstite and implications for the seismological properties of the Earth's lower mantle. J Geophys Res. doi:10.1029/2006JB004730

Tommaseo C, Devine J, Merkel S, Speziale S, Wenk HR (2006) Texture development and elastic stresses in magnesiowustite at high pressure. Phys Chem Miner 33:84–97

Wenk HR, Canova G, Molinari A, Mecking H (1989) Texture development in halite: comparison of taylor model and self-consistent theory. Acta Metall Mater 37(7):2017–2029

Wenk HR, Matthies S, Donovan J, Chateigner D (1998) BEARTEX: a Windows-based program system for quantitative texture analysis. J Appl Cryst 31:262–269

Wenk HR, Lonardelli I, Merkel S, Miyagi L, Pehl J, Speziale S, Tommaseo C (2006) Deformation textures produced in diamond anvil experiments, analyzed in radial diffraction geometry. J Phys: Condens Matter 18:S933–S947

Wenk HR, Cottaar S, Tomé C, McNamara A, Romanowicz B (2011) Deformation of the lowermost mantle: from polycrystal plasticity to seismic anisotropy. Earth Planet Sci Lett 306:33–45

Yagi T, Suzuki T, Akimoto S-I (1985) Static compression of wustite (Fe0.98O) to 120 GPa. J Geophys Res 90(B10):8784–8788

Zhuravlev K, Jackson J, Wolf A, Wicks J, Yan J, Clark S (2010) Isothermal compression behavior of (Mg, Fe)O using neon as a pressure medium. Phys Chem Miner 37:465–474

Zou G, Mao HK, Bell P, Virgo D (1979–1980). High pressure experiments on the iron oxide wustite ($Fe_{1-x}O$). Year Book, Carnegie Institute of Washington, Washington, vol 39, pp 374–376